Article

Experimental Study on PIV Measurement and CFD Investigation of the Internal Flow Characteristics in a Reactor Coolant Pump

Dan Ni [1,2,*] **, Hongzhong Lu** [1] **, Shiyuan Huang** [2] **, Sheng Lu** [1] **and Yang Zhang** [3]

[1] Shanghai Kaiquan Pump (Group) Co., Ltd., Shanghai 201800, China
[2] School of Energy and Power Engineering, Jiangsu University, Zhenjiang 212013, China
[3] Shanghai Marine Equipment Research Institute (SMERI), Shanghai 200031, China
[*] Correspondence: nidan@ujs.edu.cn

Abstract: The nuclear reactor coolant pump (RCP) is the core piece of equipment of a nuclear power plant (NPP). The energy performance and internal flow characteristics of RCPs are revealed by effective measurement methods, which are helpful to understand the flow mechanism of RCPs. The present work is intended to conduct an integrated study based on the energy performance test and Particle Image Velocimetry (PIV) flow-field non-contact measurement of the RCP. In addition, the prediction results of different turbulence models are compared with experimental results in detail. Through energy performance measurement and numerical calculation analysis, it can be found that various turbulence models have the ability to predict the performance of RCPs in engineering applications. At 0.8~1.2 Φ_d operating conditions, the maximum error is less than 10% and the minimum error is less than 0.1% by analyzing the energy performance of numerical calculations and experimental results. The PIV results show that the velocity of the discharge nozzle varies greatly from right (outlet of diffuser channel 2) to left (outlet of diffuser channel 12) due to different flow structures. Through the qualitative and quantitative comparison of the internal flow field, it can be concluded that, except for the low flow rate, compared with other computational models, the Realizable k-ε model can better predict the internal flow field of an RCP. The reasons for the experimental error and numerical calculation error are analyzed in detail, and the results can provide a reference for forecasting an RCP internal flow field with a special and complex structure.

Keywords: reactor coolant pump (RCP); internal flow characteristics; energy performance; PIV; velocity distribution; numerical calculation

1. Introduction

With the current emphasis on energy security, many countries are actively responding to decarbonization policies to cope with the harm caused by global climate change and air pollution [1,2]. Using cleaner energy to meet the growing demand for electricity is an inevitable choice [3]. In achieving the decarbonization goal, nuclear energy has an important role to play [4]; and in facing growing global demand for electric power generation, nuclear energy is likely to be the most promising research and development area [5]. It can provide stable and zero-emission electricity to complement wind energy, solar energy, hydropower and other energy sources affected by seasonal climate change. Many scholars [6–8] have conducted research on nuclear energy.

The nuclear reactor coolant pump (RCP) is an important piece of equipment in a nuclear power plant (NPP) and thus plays a decisive role. The RCP is the only long-term high-speed rotating device in the primary system, which is used to drive the coolant circulation in the primary circuit to achieve the heat transfer between the reactor core and the steam generator. Therefore, it is necessary to ensure its safe, reliable and efficient long-term operation [9]. Considering the particularity of the working environment, the

arduousness of the work task and the sustainability of the working time in industrial production, the RCP has a larger spherical casing compared with the traditional pump [10]. The spherical casing has the advantages of good bearing safety, high strength and easy processing. However, due to the special spherical casing structure of the RCP, its energy performance is low and the internal flow structure is complex [11]. Therefore, it is necessary to restore its complex internal unsteady flow structure, capture its large-scale high energy consumption structure, find the main source of loss, and reveal the nature of its internal flow and energy loss mechanism. It is of great significance to improve the operation efficiency and safety of RCPs in engineering.

An accurate test method is vital to reveal the complex flow in the pump. Particle Image Velocimetry (PIV) [12,13] and Laser Doppler Velocimetry (LDV) [14,15] are widely used to measure the complex flows in pumps because of their non-contact characteristics and lack of effect on the flow field. Wu et al. [16] used PIV to measure the internal flow field of a centrifugal pump under design conditions. Edgar M. et al. [17] used two-dimensional PIV to study the flow of different planes in centrifugal pumps at different speeds and working conditions. By analyzing the parameters of pressure, velocity, Reynolds shear stress and turbulence intensity, it is shown that the flow in the centrifugal pump has kinematic similarity even under partial load conditions. Pedersen N et al. [18] used PIV and LDV to measure the flow channels in the centrifugal impeller rotating region in detail, and the comparison of the mean field results obtained by PIV and LDV tests showed good consistency. Daisuke S et al. [19] studied a high-head pump with an unshrouded impeller. LDV was used to measure the velocity distribution at the inlet and outlet plane of the diffuser and to capture the flow from the unshrouded impeller. They evaluated the relationship between total pressure and velocity distribution. The experimental results were compared with the computational fluid dynamics simulation results, and the phenomenon where the streamline moves to the shroud side was verified. They believe that the ununiform flow in the diffuser was caused by the influence of the secondary flow in the unshrouded impeller.

The rapid development of Computational Fluid Dynamics (CFD) has brought convenience to the performance and flow field prediction of pumps [20,21]. Chun-Yan Ge et al. [22] systematically studied the hydrodynamic characteristics under the pump mode of the improved paddle turbine by using PIV and CFD technology. The average axial and radial velocity and turbulent kinetic energy simulated by the standard k-ε turbulence model were verified using measured PIV data. The results showed that the standard k-ε model could predict the mean velocity well, but turbulent kinetic energy near the blades was underestimated. Li H. et al. [23] studied the internal flow at the trailing edges of the blades of different impellers to explore the influence of their shape on the performance by CFD. The energy loss and vortex structure were analyzed by using entropy production theory and vortex identification method. The research results are helpful to further understand the complex flow mechanism of centrifugal pump.

To study the transient flow structure and pressure pulsation characteristics of a centrifugal pump under off-design conditions, the Delayed Detached Eddy Simulation (DDES) method was adopted by Zhang et al. [21]. The focus was on the transient evolution of the vortex structure and pressure pulsation under stall conditions, and the reliability of the numerical calculation was verified through experimental PIV data.

In recent years, researchers have used experimental and computational fluid dynamics (CFD) methods to measure the internal flow field of centrifugal pumps [12,24–26], most of which focus on single-stage spiral volute centrifugal pumps [27–29]. There are few studies of RCP, especially the internal flow field measured by the visualization test. For the RCP with a special spherical casing structure, its internal complex flow structure and energy form need to be studied and revealed. Therefore, the combination of experiment and computational fluid dynamics by non-contact PIV technology can fully reveal the internal flow and energy loss law of RCP, provide ideas and theoretical support for the design and development of efficient and stable RCP. In addition, the roughness effect [30] should be paid attention to when studying RCP.

This paper studies the energy performance and internal flow characteristics under main operating conditions on the basis of non-contact measurement in the RCP. Based on the experimental results and the CFD numerical simulation method, the error between the test and the numerical calculation is analyzed, and a better turbulence model is obtained. The research results can provide a useful reference for predicting the internal flow field of the RCP with a special and complex structure accurately in the future.

2. Experimental Setup

2.1. RCP and Test Rig

The prototype pump is a nuclear reactor coolant pump used in a Pressurized Water Reactor (PWR) nuclear power unit. The scale ratio between the prototype pump and the model pump is 3:1. The dimensionless experimental parameters of the model pump RCP are shown in Table 1. Hydraulic components of the RCP include inlet nozzle, impeller, diffuser, guide ring, spherical casing and outlet nozzle, as shown in Figure 1. Diffuser, spherical casing and outlet nozzle use a plexiglass material because of the requirement of the visualization function in RCP by the non-contact PIV test.

Table 1. Parameters of the testing RCP.

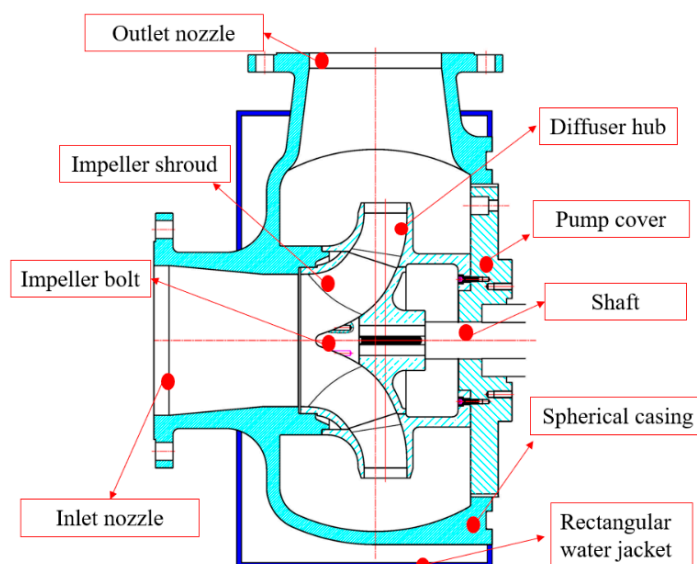| Parameters	Value
Nominal flow coefficient Φ_d	$Q_d/(u_2 R_2{}^2) = 0.63$
Nominal head coefficient Ψ_d	$gH_d/u_2{}^2 = 0.25$
Nominal rotating speed n_d	900 r/min
Specific speed n_s	$n\sqrt{Q_d}/H_d{}^{0.75} = 107$ (n: min^{-1})
Impeller inlet diameter D_1	221 mm
Impeller outlet diameter D_2	268 mm
Impeller outlet width b_2	84 mm

Figure 1. Details of the model RCP.

The performance test and PIV visualization measurement of the model RCP are conducted on the closed test rig, and the schematic diagram of the test equipment is shown in Figure 2. During the experiment, the water temperature is maintained at about 25 °C. The function of the storage tank in the system is to stabilize the inlet flow. Two pressure gauges are installed in the test system to measure the pump head, and they are located at the inlet

nozzle and outlet nozzle of the model pump. The accuracy of the pressure gauges is $\pm 0.1\%$. During the test, the flow rate is changed to measure the performance of the pump under different working conditions. The change of flow rate is measured by a high-precision electromagnetic flowmeter with a measuring accuracy of $\pm 0.2\%$. A frequency converter is used to keep the speed of the model pump constant in the experiment.
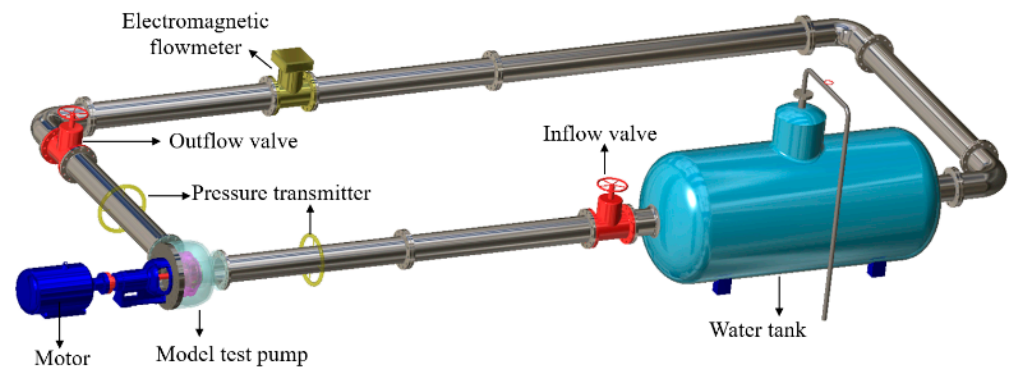

Figure 2. Schematic of the experimental setup.

2.2. PIV Measurement Setup

The 2D2C particle image velocimetry measurement system produced by Dantec Dynamics A/S is used to build the time-averaged flow-field testing platform for model pump visualization, which is based on the Dynamic Studio intelligent software platform V4.10. Nd-YAG laser is used as the laser source, which can emit continuous pulses of light with a wavelength of 532 nm, energy of 60 mJ per pulse and pulse width of 15 ns. The maximum frequency of the obtained pattern is 15 Hz. To ensure that the particle displacement meets the imaging requirements, the pulse laser interval is selected as 50 µs according to the measured flow field velocity.

The optical elements in the test include a cylindrical mirror and a spherical mirror. The collimated laser beam diverges in one direction after passing through the cylindrical mirror, so that the laser beam forms a flake light source to illuminate the measured area, and the spherical mirror is used to control the thickness of the flake light source.

A Flow Sense EO 2 M CCD camera, with a spatial resolution of 1600×1200 pixels and a pixel size of 7.4 microns, is used to record the motion path of tracer particles. The lens used in the test system is a Nikon lens, model AF Nikkor 50 mm f/1.8. In the measurement process, the laser emission is synchronized with the exposure time of the CCD camera, and the camera is perpendicular to the laser plate to improve the measurement accuracy.

For the configuration of the PIV system in this experiment, according to the principles observed by the PIV measurement and the velocity of the flow field in the pump, the interrogation window is a point of dimensions 32×32 pixels. For the interrogation window with 50% overlap, the cross-correlation algorithm is used to extract the velocity, and the vector resolution is 1.7 mm. For the selection of particles in the PIV measurement, in addition to ensuring its non-toxicity, no corrosion, no wear, chemical stability, cleanliness and other requirements, considering they would follow the fluid to reflect the real fluid movement and its scattering to facilitate photographic imaging, a hollow glass sphere with a diameter of 20~60 µm and a density of 1050 kg/m^3 was used as the tracer particle. The distribution and concentration of particles in the fluid ensure that at least 4 to 20 pairs of tracer particles can be captured in each interrogation window to meet the requirement of obtaining the whole flow field image information.

In this experiment, five sections perpendicular to the axis and centered on the impeller and diffuser outlet were selected for shooting and were defined as Z1~Z5 from the diffuser shroud to the hub. On each section, the shooting area of the flow field is the fluid region from each diffuser exit to the spherical casing, which is defined as diffuser channel 2~12. In each measurement area, 300 sets of images were taken in double-frame and double-

exposure mode to obtain the average velocity. The experimental error of PIV is within 3%, which is within the allowable range of the test. The PIV measurement is shown in Figure 3.
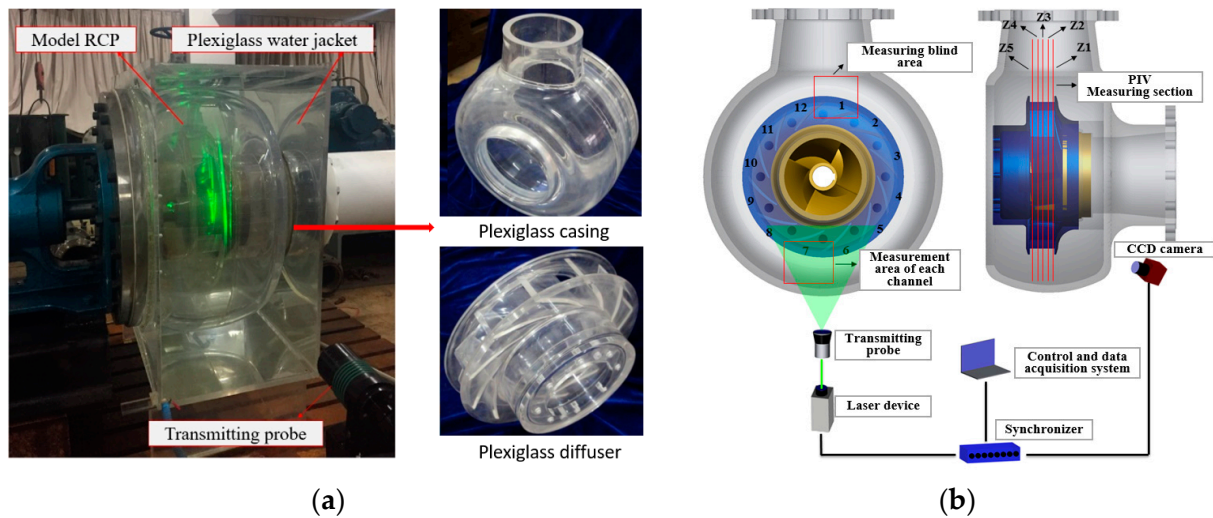

(**a**) (**b**)

Figure 3. PIV measurement. (**a**) PIV measurement system; (**b**) schematic diagram of PIV measurement scheme.

3. Numerical Methodology and Setting

3.1. Computational Domain

During the numerical simulation, a three-dimensional full-flow channel is used. The calculation domain is consistent with the actual experimental model RCP, including the static domain (inlet, diffuser channel, spherical casing and outlet flow domain) and rotation domain (impeller flow domain). The computational domain is shown in Figure 4.
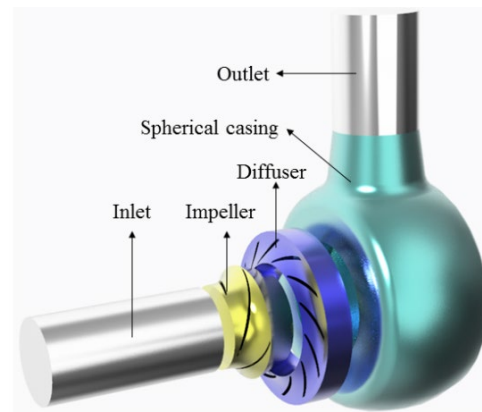

Figure 4. Computational flow domain.

3.2. Turbulence Models and Numerical Method

3.2.1. Turbulence Models

The measurement method adopts the PIV time-averaged flow-field measurement method. The measurement results are average flow-fields information. Therefore, when considering the choice of numerical methods, the Reynolds average method is chosen for reliable comparison with experimental results. This method is to perform Reynolds average processing on the physical quantities of the flow field in the time domain, and then solve the time-averaged governing equation. The core of this method is to process the Navier–Stokes equation with the aid of the averaging mode, and then construct the Reynolds-Averaged Navier–Stokes equation (RANS) [31]. This method has high computational efficiency and wide-ranging engineering applications. In this paper, according to different assumptions or

treatments of Reynolds stress, two of the currently most widely used turbulence models are discussed, including the two series of two-equation eddy viscosity models of *k-ε* and *k-ω* and the Reynolds Stress Model (RSM).

The numerical models are implemented by directly selecting in ANASY FLUENT. The *k-ε* model discussed in this paper includes the Standard *k-ε* model [32], RNG *k-ε* model [33] and Realizable *k-ε* [34] model. The *k-ω* model discussed mainly includes the Wilcox *k-ω* model (Standard *k-ω* model) [35], Baseline *k-ω* model (BSL *k-ω* model) and Shear Stress Transport *k-ω* model (SST *k-ω* model) [36]. The advantage of RSM lies in its high calculation accuracy, which is especially suitable for problems with large streamline curvature and high rotation strength; however, its calculation amount is relatively large. In this paper, RSM of Linear Pressure-strain (RMS-LPS) is adopted. Since the selected models are all mature models used in the engineering field, this paper will not introduce them in detail.

3.2.2. Numerical Method

Ansys-Fluent is used to simulate the full three-dimensional flow field of the model RCP. We discretized the filtered governing equations based on the finite-volume scheme. Through the SIMPLEC algorithm, the coupling relationship between pressure and velocity is established. To compare and find an excellent turbulence model suitable for predicting the energy performance and internal flow structure of the model RCP, Standard *k-ε*, Realizable *k-ε*, RNG *k-ε*, Standard *k-ω*, BSL *k-ω*, SST *k-ω* and RMS-LPS are used in the calculation. The discrete scheme adopts the second-order upwind scheme. For the *k-ε* model and the RMS-LPS model, the near-wall surface is processed by the standard wall function. The inlet boundary condition is set as a uniform velocity inlet, and its value is given according to the operating conditions. In the inlet boundary conditions, specific turbulence characteristics are given, in which the turbulence intensity is given 5%, and the hydraulic diameter is set as the impeller inlet diameter. The outlet boundary condition is set as a pressure outlet, which is given as atmospheric pressure (p = 101,325 Pa). All the physical walls of the hydraulic components in the model RCP are set as non-slip walls. The Moving Reference Frame (MRF) model is applied in the rotating domain to perform steady-state numerical calculations.

3.3. Independence Test of Mesh Density

The quality of the mesh determines the accuracy of the numerical calculation. The structured mesh has smaller truncation errors and better convergence characteristics during the entire numerical simulation process. Therefore, this paper chooses structured hexahedral mesh generation technology (Ansys—ICEM mesh generation tool) to mesh all the computational domains of the model RCP. To ensure the accuracy of the calculation, mesh refinement is performed in areas where there is a large pressure gradient and flow separation is more likely to occur, especially on the surface of the blade. The structured mesh of the impeller and diffuser in the model RCP are shown in Figure 5.

Considering the accuracy of the calculation as well as the computing power and the CPU time of the computer, to ensure that the grid has sufficient analytical accuracy for the flow field, the mesh independence of the whole flow domain is verified. Six different grid number schemes have been designed. All different turbulence models are calculated with the same mesh, and the mesh-independent verified turbulence model is RNG *k-ε*. In the calculation, the error convergence is good, which can reach the order of 10^{-5}. At the same time, the head coefficients corresponding to the six schemes are monitored, and the effect of the mesh number on the energy performance of the model RCP is studied as shown in Figure 6. Figure 6 shows the head coefficients under the same operating conditions with different mesh numbers. It can be seen from Figure 6 that the head coefficient gradually decreases and stabilizes with an increase in the number of grids. When the number of grids increases to scheme 4, the head coefficient basically does not change. It is considered that the number of grids increases does not affect the energy performance of RCP after scheme 4. Considering the economic efficiency of the calculation, case 4 is selected as the final

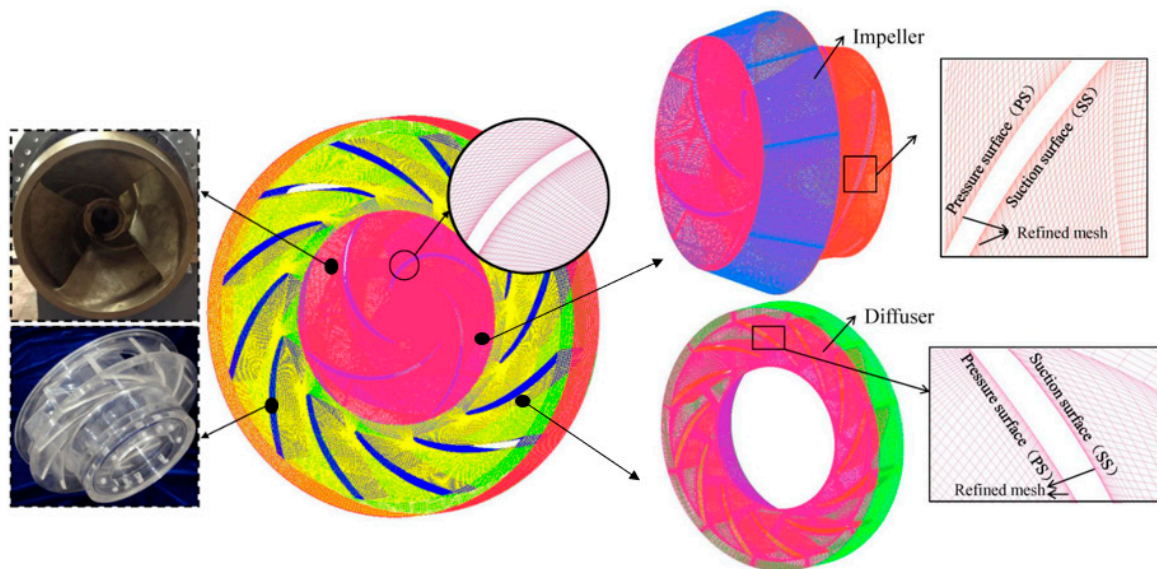calculation solution. The total number of grids is 74,38,559, and the number of impeller grids is 3,231,400.

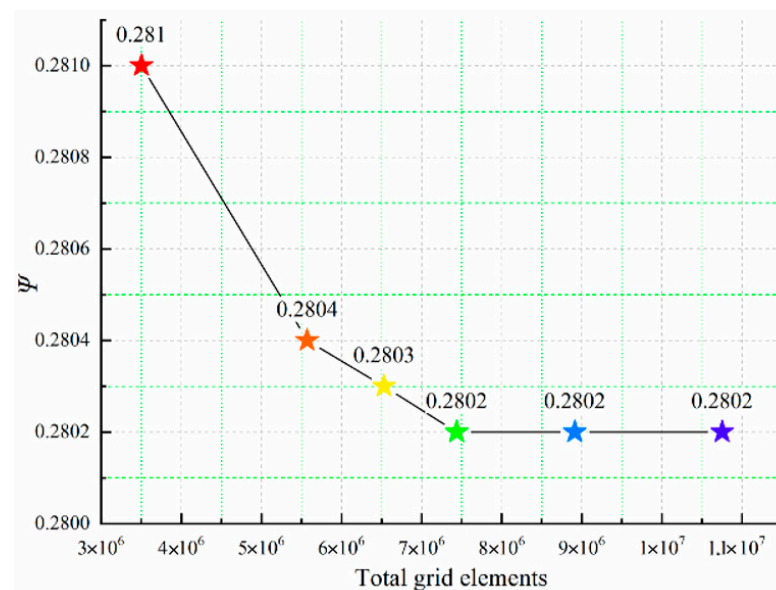**Figure 5.** Structured mesh of impeller and diffuser in the RCP.

Figure 6. Mesh sensitivity check.

4. Result and Discussion

4.1. Energy Performance Analysis

The energy performance is an important external characteristic of measuring the error of experimental results and numerical results. Therefore, the energy performance of the numerical calculation results with different turbulence models is compared with the experimental results, and Figure 7 shows the comparison of energy performance. In general, the error of head coefficient Ψ between numerical simulation and experiment is small. The results of the different turbulence models are consistent. The head coefficient Ψ calculated by the numerical simulation is generally slightly higher than the experimental value. Because the errors of energy performance between the different turbulence models are small, Tables 2–4 list the errors of the different RANS methods relative to the experimental values under three different flow rates.
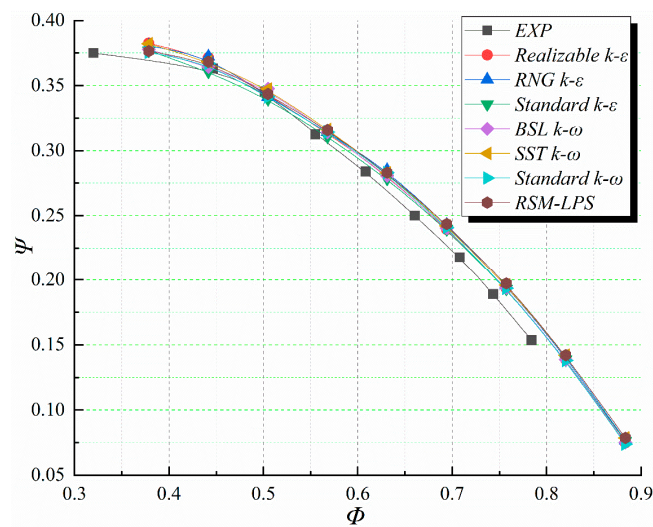
Figure 7. Energy performance comparison between experimental and numerical results.

Table 2. Energy performances between experiment result and different RANS methods at Φ_d.

Method	Φ_d	Ψ	Error (%)
EXP	0.63	0.269	0
Standard *k-ε*	0.63	0.279	3.58
Realizable *k-ε*	0.63	0.282	4.61
RNG *k-ε*	0.63	0.285	5.61
Standard *k-ω*	0.63	0.283	4.95
BSL *k-ω*	0.63	0.281	4.27
SST *k-ω*	0.63	0.283	4.95
RMS-LPS	0.63	0.283	4.95

Table 3. Energy performances between experiment result and different RANS method at 0.8 Φ_d.

Method	0.8 Φ_d	Ψ	Error (%)
EXP	0.504	0.3431	0
Standard *k-ε*	0.504	0.3397	−1.00
Realizable *k-ε*	0.504	0.3428	−0.08
RNG *k-ε*	0.504	0.3414	−0.50
Standard *k-ω*	0.504	0.3413	−0.53
BSL *k-ω*	0.504	0.3476	1.29
SST *k-ω*	0.504	0.3474	1.24
RMS-LPS	0.504	0.3436	0.15

Table 4. Energy performances between experiment result and different RANS methods at 1.2 Φ_d.

Method	1.2 Φ_d	Ψ	Error (%)
EXP	0.756	0.178	0
Standard *k-ε*	0.756	0.193	7.77
Realizable *k-ε*	0.756	0.193	7.77

Table 4. *Cont.*

| Method	1.2 Φ_d	Ψ	Error (%)
RNG k-ε	0.756	0.196	9.18
Standard k-ω	0.756	0.194	8.24
BSL k-ω	0.756	0.194	8.24
SST k-ω	0.756	0.196	9.18
RMS-LPS	0.756	0.197	9.64
RMS-LPS	0.756	0.197	9.64

Table 2 shows the errors in energy performance at the nominal flow rate (Φ_d). It can be seen from the table that the error between the energy performance of the Standard k-ε model and the experimental result is the smallest, at 3.58%. The error between the calculated result of the RNG k-ε model and the experimental result is relatively large, at 5.61%. Table 3 shows the error in energy performance under a 0.8 Φ_d flow rate. The error result is smaller than that of the nominal flow rate (Φ_d), and the error between the Realizable k-ε model and the experimental result is the smallest, at −0.08%. The error of the BSL k-ω model is relatively large, at 1.29%. In general, the energy performance error calculated by numerical calculation and measured by experiment is fairly small under low flow rate (0.8 Φ_d). The error in energy performance under a 1.2 Φ_d flow rate is listed in Table 4. It can be seen from the table that the error results are greater than the other flow rates. The numerical results of the Realizable k-ε and Standard k-ε models showed the smallest error of 7.77%. The RMS-LPS model has a relatively large error of 9.64% compared with the experimental results.

It is important to note that under a large flow rate (1.2 Φ_d), the numerical calculation results are larger than the experimental results. Due to the complexity of the internal flow of the RCP, the RANS method averages more complex details of the flow, especially in the flow separation area, which makes the external energy performance error larger. On the other hand, the influence of the impeller ring gap flow and leakage on the energy performance of the RCP is ignored in the numerical calculation process to simplify the model. With an increase in the flow rate, the leakage will increase, and the errors between the RANS method and the experiment will increase. Therefore, this is also the reason why the error is small when operating at a low flow rate.

In summary, the main operating conditions of the RCP are 0.8~1.2 Φ_d. According to the analysis of the energy performance error in this operating interval, the maximum error is less than 10%, and the minimum error is less than 0.1%. Thence, the turbulence models discussed in this paper can predict the external energy performance of the RCP in an engineering application, and the internal flow errors are worthy of further analysis.

4.2. Flow Field Details in PIV Measurement

The time-averaged flow field measured by PIV is used for image processing based on the Intelligent Software Platform V4.10 of Dynamic Studio. The time-averaged velocity fields of different diffuser flow channel measurement areas (diffuser flow channel 2~12) and different measurement sections (Z1~Z5) of the RCP under main operating conditions (0.8~1.2 Φ_d) are obtained. This section focuses on the analysis of the flow in the four main diffuser channels under the nominal flow rate (Φ_d) at different measurement sections. Figure 8 displays the internal velocity and streamline distribution of diffuser flow channel 2, channel 6, channel 9 and channel 12 in five different measurement sections at the nominal flow rate.

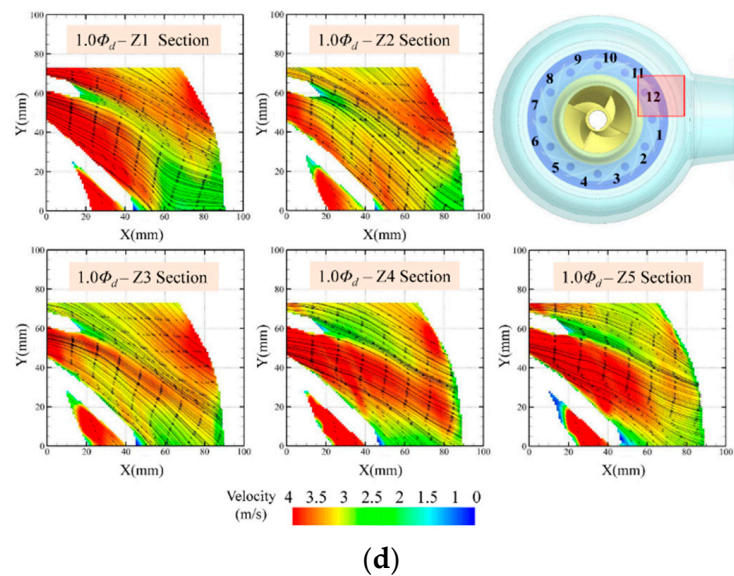(**a**)

(**b**)

(**c**)

Figure 8. *Cont.*

(d)
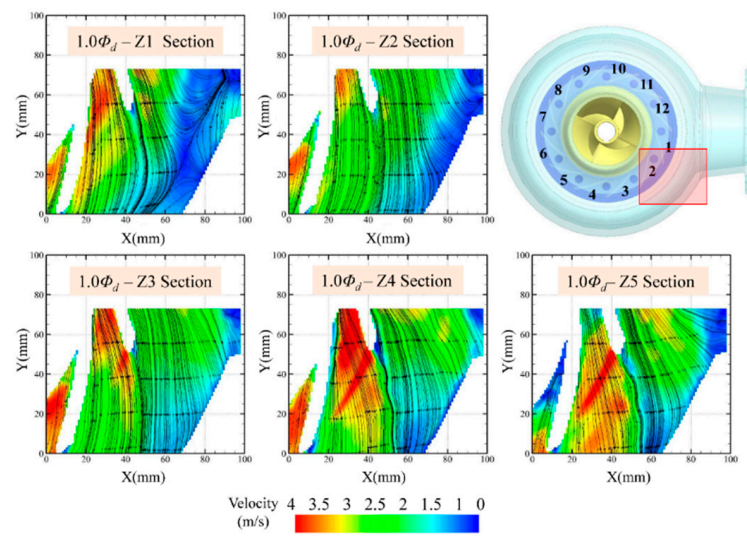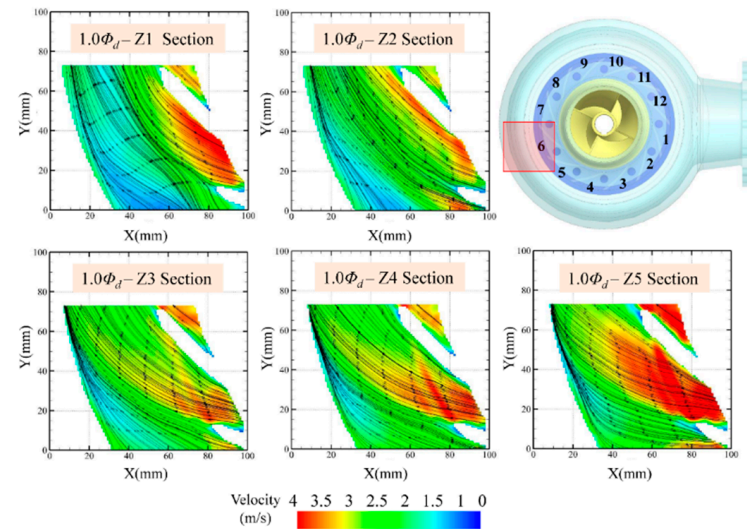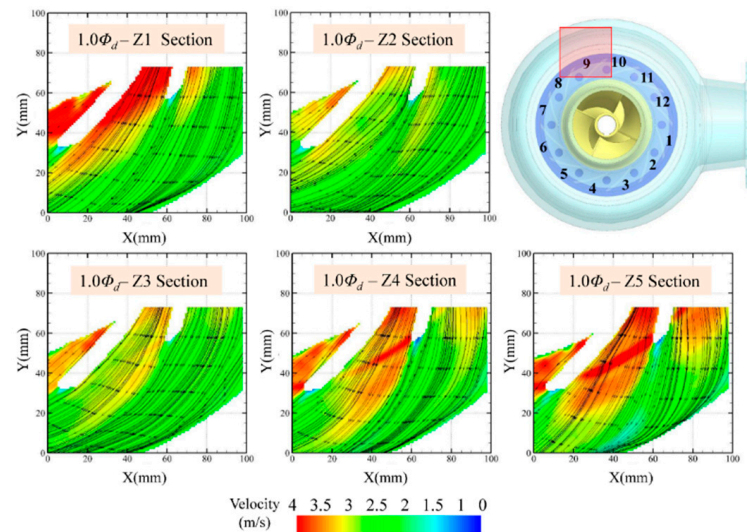
Figure 8. Internal velocity cloud map and velocity streamline distribution of five measuring sections under 1.0 Φ_d in PIV measurement. (**a**) Diffuser flow channel 2; (**b**) Diffuser flow channel 6; (**c**) Diffuser flow channel 9; (**d**) Diffuser flow channel 12.

From Figure 8a, the actual flow field in the diffuser flow channel 2 shows that large-scale flow separation is found due to the influence of the discharge nozzle, especially at the measuring section Z1 near the diffuser shroud under the nominal flow rate (Φ_d). The large-scale flow separation is the main reason for energy loss in the spherical casing [10,37]. Meanwhile, under this working condition, the flow situation here is relatively good; no large vortex structure and backflow are found, and the run-through flow and circulating flow can flow out well. However, it is important to note that there are significant velocity fluctuations at the trailing edge of the diffuser blade, which should be caused by the periodic shedding of a Karman vortex at the diffuser blade trailing edge [38].

From Figure 8b, the actual flow field inside the diffuser flow channel 6 can be obtained at the nominal flow rate. The velocity in this channel is larger near the diffuser shroud (Z1) and hub (Z5), while the velocity distribution in the middle section (Z2~Z4 section) is more uniform. As can be seen from the streamline distribution, the fluid flowing out of the diffuser flow channel 6 and the fluid flowing out of the previous channel converge at the bottom of the spherical casing, and then collide against the bottom wall of the spherical casing together.

Figure 8c shows the velocity distribution of the diffuser flow channel 9. It should be noted that the internal flow diagram of flow channel 9 is a mirror image of the actual measurement position, not an error in the measurement area. It can be found that the velocity gradually decreases and then gradually increases from the diffuser shroud to the hub. In addition, the velocity distribution in the middle section is more uniform. As can be seen from the streamline distribution, the fluid flowing out of the diffuser flow channel 9 and the fluid flowing out of the previous flow channel converge on the left side of the spherical casing and collide against the left wall. Compared with the flow field distribution of the diffuser flow channel 6, the fluid at the diffuser flow channel 9 still converges and squeezes toward the spherical casing wall, but the flow here is relatively smooth.

The internal velocity cloud map and velocity streamline distribution of the diffuser flow channel 12 (near the discharge nozzle) are shown in Figure 8d. The velocity distribution in the diffuser flow channel 12 still gradually decreases and then increases from the diffuser shroud to the hub, and the velocity distribution is more uniform at the middle section. However, combining the velocity distribution of the diffuser flow channel 2 (Figure 8a), it can be concluded that the velocity difference between the left and right sides of the discharge nozzle is relatively large. On the right side of the discharge nozzle (diffuser

flow channel 2), the flow speed is slower and uneven due to the influence of the vortex, backflow and large-scale flow separation structure. On the left side of the discharge nozzle (diffuser flow channel 12), the fluid flows out of the discharge nozzle smoothly under the action of the main flow, so the velocity distribution is relatively uniform and there is no obvious low-speed area.

4.3. Comparative Analysis between CFD and PIV

Through PIV flow field measurement, the detailed and comprehensive time-averaged flow field under the main operating conditions of RCP are obtained. To further verify the accuracy of the numerical calculations, this section is based on the PIV measurement results, the numerical results of the RANS method are preliminarily analyzed and compared. In addition, the results provide a basis for further optimization of the numerical calculation method.

Two measurement sections are selected for comparison and analysis. Figure 9a shows the location of the measurement target area, including two diffuser flow channels. One area is named diffuser flow channel 5, and is the main flow area with a relatively simple flow. The other one is defined as diffuser flow channel 2, which is the flow separation area with a more complicated flow. Figure 9b,c are the measurement area and the monitoring line of the diffuser flow channel 5 and the diffuser flow channel 2, respectively. X = 35, X = 55 and X = 75 are selected in diffuser flow channel 5, and X = 55, X = 65 and X = 75 are selected in diffuser flow channel 2.
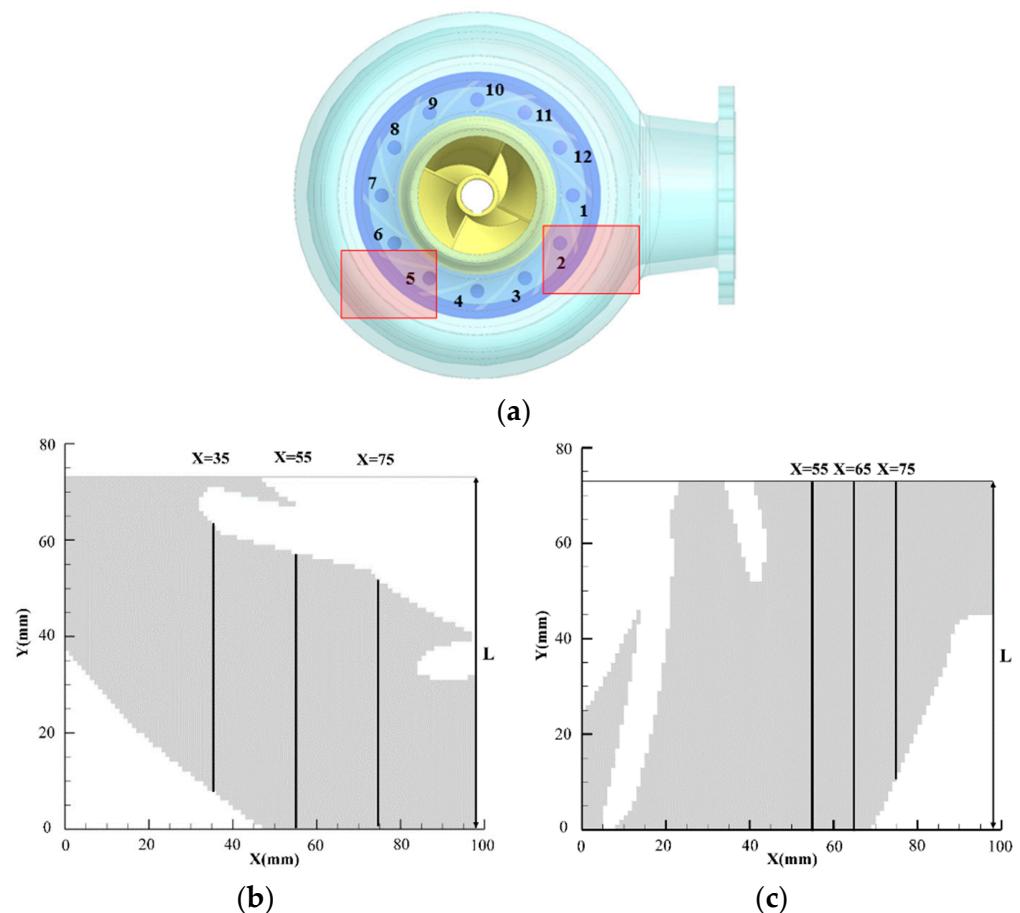

(a)

(b)　　　　　　　　　　　　　　　　　　　　(c)

Figure 9. Positions of the target area (diffuser flow channel 5 and channel 2). (**a**) The target area; (**b**) monitoring line of the diffuser flow channel 5; (**c**) monitoring line of the diffuser flow channel 2.

Preliminary studies and PIV measurement results have shown that the flow in the diffuser flow channel 5 is relatively simple, and the main flow is through-flow [39]. Therefore, the PIV measurement result of the flow field in the diffuser flow channel 5 is compared with

the RANS results. Figure 10 shows the internal velocity distribution of experiment results and different RANS methods at the Z3 section under three main operating conditions. From the velocity flow field at the nominal flow rate in Figure 10a, it is obvious that there is a local high-speed area in the middle of diffuser flow channel 5. According to the PIV measurement results, this local high-speed area appears as a "corrugated belt" and is not continuous. In the previous unsteady numerical research, the instability phenomenon of the "corrugated belt" in the diffuser flow channel has been found [13]. However, the RANS method cannot capture this kind of speed fluctuation phenomenon well. From the perspective of large-scale flow characteristics, the internal flow field calculated by the *k-ε* model (Standard *k-ε*, Realizable *k-ε*, RNG *k-ε*) is relatively consistent with the experimental result. The standard *k-ω* model and RSM-LPS model also have a better ability to capture local high-speed areas. However, the flow field predicted by the BSL *k-ω* model and the SST *k-ω* model are quite different from the experimental results, and the flow in this area cannot be accurately predicted.
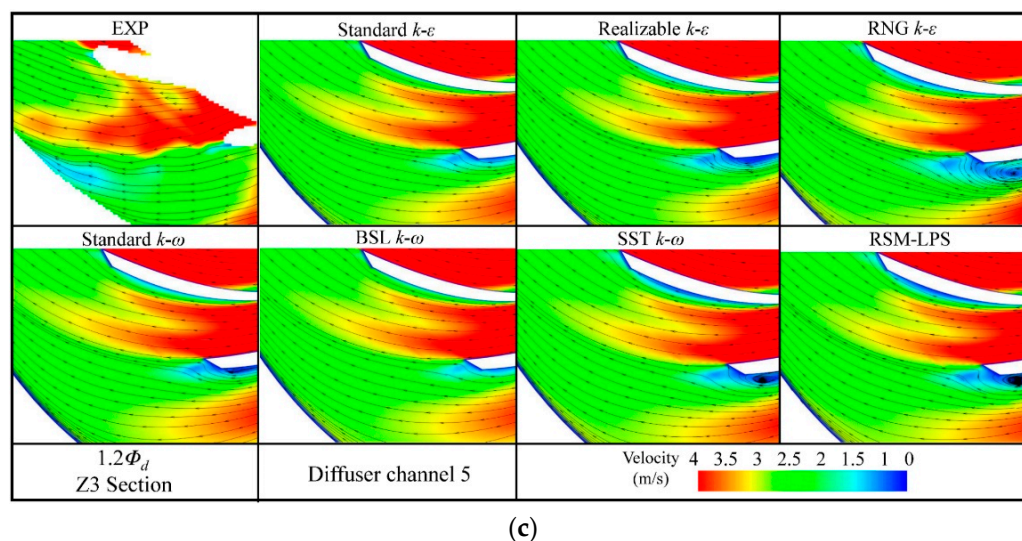

(**a**)

(**b**)

Figure 10. *Cont.*

(c)
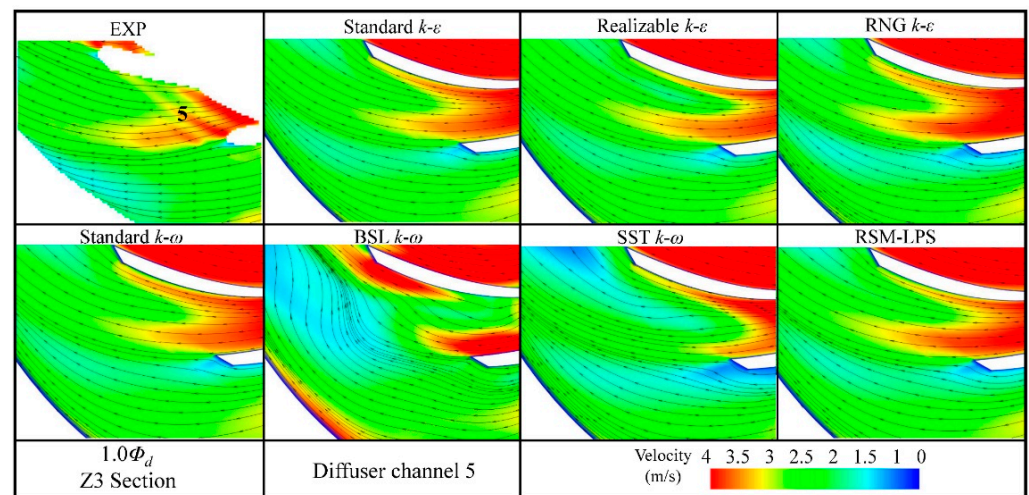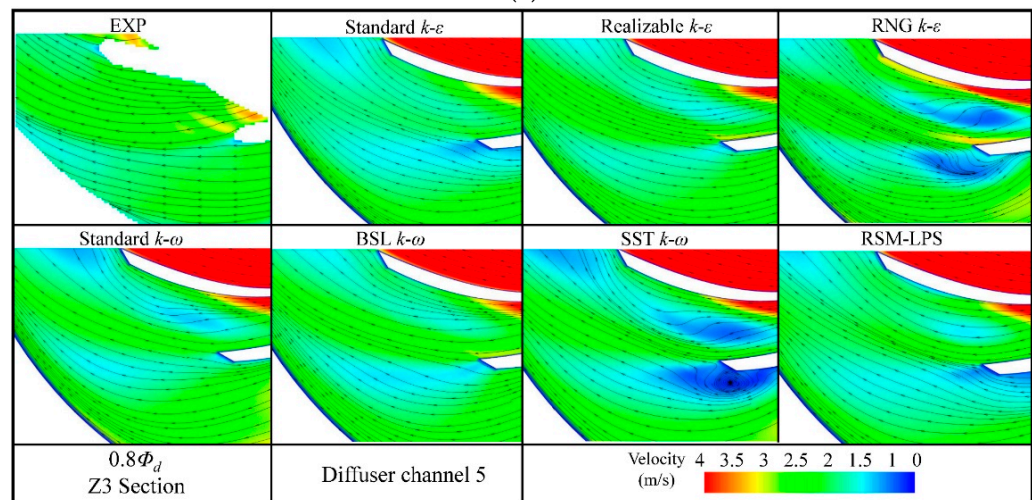
Figure 10. Internal velocity distribution of experimental results and different RANS methods at the Z3 section in the diffuser flow channel 5. (**a**) 1.0 Φ_d; (**b**) 0.8 Φ_d; (**c**) 1.2 Φ_d.

From the velocity flow field at 0.8 Φ_d in Figure 10b, it can be analyzed that when the RCP is operating at a relatively low flow rate, there is no obvious local high-speed area in the diffuser flow channel 5 measured by the experiment. The distribution is relatively uniform, and local low-speed areas appear on the trailing edge of the diffuser blade and the wall of the spherical casing. From the RANS method results, it can be found that the numerical calculation results cannot accurately capture the velocity distribution in this flow channel. Among them, the flow fields predicted by the RNG k-ε model and the SST k-ω model are clearly resolved in the flow channel and at the trailing edge of the diffuser blade. Thus, in the low-speed area, this is obviously inconsistent with the test results. By comparison, the Realizable k-ε model is relatively better analytical model for the flow field under 0.8 Φ_d.

Figure 10c shows the velocity flow field at 1.2 Φ_d; it can be seen from the figure that when the RCP runs to a relatively large flow rate, the local high-speed area in the diffuser flow channel 5 is more obvious, and the high-speed area occupies almost the entire flow path. At the same time, the "corrugated belt" in the high-speed area is more obvious. From the RANS method results, it can be found that the numerical calculation results are more accurate for the analytical ability under a large flow rate. Although this "corrugated belt" high-speed area cannot be accurately captured, the mainstream velocity distribution is in good agreement. Among them, the Standard k-ε model and the BSL k-ω model are in good agreement with the experimental results. Other RANS models have resolved obvious local vortices at the trailing edge of the diffuser blade, which is inconsistent with the experimental results.

From a quantitative point of view, velocity comparison and analysis on the monitoring lines are essential. Therefore, Figure 11 shows the velocity distribution on the three main monitoring lines in the diffuser flow channel 5 under the nominal flow rate (1.0 Φ_d). The abscissa represents the velocity and the ordinate is the ratio of the Y axis to the height L of the measurement area, which is a dimensionless coordinate.

It can be seen from Figure 11a that when X = 35, in the area of $0.45 \leq Y/L \leq 0.65$ (local high-speed area), the velocity distributions calculated by the k-ε model (Standard k-ε, Realizable k-ε, RNG k-ε), Standard k-ω and RSM-LPS model are relatively consistent with the experimental results. However, in the areas of $Y/L \leq 0.4$ and $Y/L \geq 0.7$, the trends of the numerical simulation results and test results are inconsistent. Therefore, it is considered that the capturing ability of the RANS method becomes weak near the wall, which may be related to the wall function or the grid.
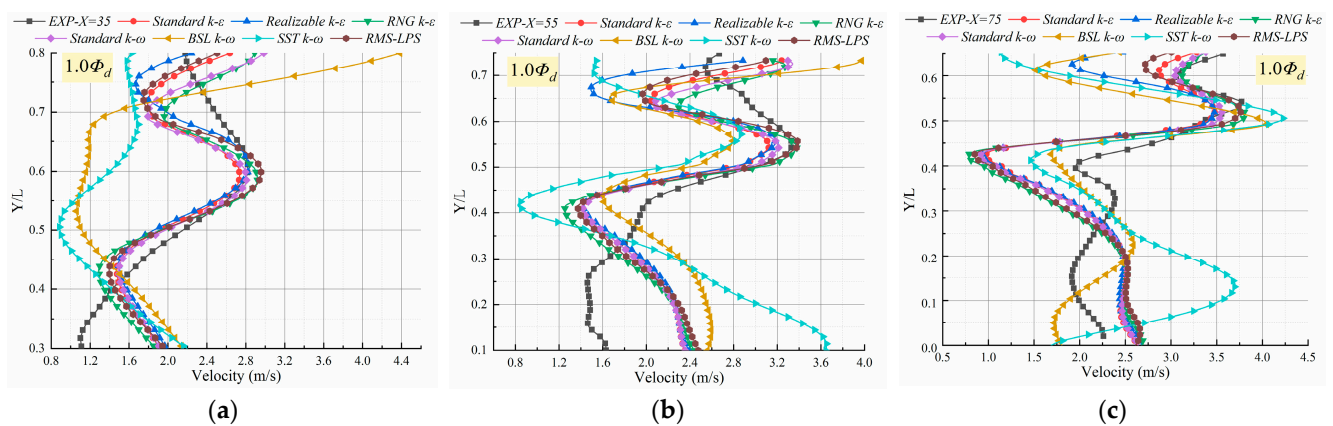
Figure 11. Velocity distribution of monitoring line with diffuser channel 5 under 1.0 Φ_d. (**a**) X = 35; (**b**) X = 55; (**c**) X = 75.

When X = 55, it can be found from Figure 11b that in the area of $0.45 \leq Y/L \leq 0.6$, for the BSL k-ω model and SST k-ω model, there is still a large difference between the experimental measurement value. Meanwhile, the other turbulence models are consistent with the basic trend of the experimental values. However, in the area of $Y/L \leq 0.45$ and $Y/L \geq 0.6$, the trends of different turbulent models and test results are still inconsistent. When X = 75 (Figure 11c), the overall velocity fluctuates greatly. In the area of $Y/L \geq 0.35$, the velocity trends of each turbulence model and the experimental value are basically the same, but there are still differences in velocity values. In the area of $Y/L \leq 0.35$, the test value is less than the calculated value, and the trend is not consistent.

Based on the analysis of Figures 10 and 11, for the main flow in the diffuser and spherical casing of the RCP, the k-ε model (Standard k-ε, Realizable k-ε, RNG k-ε), Standard k-ω and RSM-LPS model have basically the same analytical capabilities for internal flow fields at the nominal flow rate. However, the flow fields predicted by the BSL k-ω model and the SST k-ω model are quite different from the experimental measurement results. At 0.8 Φ_d, the flow field predicted by the numerical calculation is quite different from the measurement result, and the analytical capability of the low-speed area is enlarged. Therein, the Realizable k-ε model is relatively consistent. At 1.2 Φ_d, the ability of numerical calculation to analyze the local low-speed area of the trailing edge of the diffuser blade is enlarged, but the identification of the mainstream high-speed area is in good agreement with the test. Comprehensive analysis found that the k-ε model has obvious advantages over the k-ω model and the RSM model. Particularly, the Realizable k-ε model can better analyze the flow field in the diffuser flow channel 5.

Preliminary studies have shown [10,38] that the flow near the diffuser flow channel 2 and the discharge nozzle is the most complicated, where there is large-scale flow separation, vortex shedding and so on. Thus, PIV measurement results of the flow field in this channel are further selected and different RANS method numerical calculation results are compared and verified. Figure 12 shows the internal velocity distribution of experiment results and different RANS methods at Z3 section in diffuser flow channel 2 under three main operating conditions. From the velocity flow field at the nominal flow rate in Figure 12a, it is obvious that the local low-speed area appears near the discharge nozzle and the wall of the spherical casing. Because the fluid here is restricted by the spherical casing wall, the flow separation phenomenon is found. It is pity that due to the limitation of the position of the discharge nozzle, the entire flow field in the discharge nozzle cannot be measured by PIV. In the middle of the diffuser flow channel 2, the local high-speed area similar to a "corrugated belt" is still measured. Obviously, the RANS method averages this instability. Through the comparison of the RANS method and the experimental measurement results, it is found that the RANS method cannot effectively predict the local complex flow field inside the RCP. The k-ε model (Standard k-ε, Realizable k-ε, RNG k-ε), Standard k-ω and RSM-LPS models are relatively good for mainstream speed analysis. From the streamline distribution,

it can be found that these RANS methods clearly identify the vortex-shedding structure of the trailing edge of the diffuser blade, but the experimental results show that there is no obvious vortex-shedding structure here. The flow field predicted by the BSL *k-ω* model and the SST *k-ω* model are quite different from the experimental results, and the flow at diffuser flow channel 2 and the discharge nozzle cannot be accurately predicted.

From the velocity and flow field at 0.8 Φ_d in Figure 12b, it can be analyzed that when the RCP is operating at a relatively low flow rate, in the measurement results, an obvious low-speed area appeared at the diffuser flow channel 2 and the discharge nozzle; and a more obvious vortex structure appeared at the trailing edge of the diffuser blade. From the RANS method calculation results, it can be found that the numerical calculation results cannot accurately capture the velocity distribution in the diffuser flow channel, which is quite different from the experimental measurement results.

Figure 12c shows the velocity flow field at 1.2 Φ_d. It can be seen from the figure that the local high-speed area in diffuser channel 2 is more obvious when the RCP is operating under the relatively large flow rate. The high-speed area occupies almost the entire flow channel. The trailing edge of the diffuser blade also showed an obvious vortex-shedding structure. From the RANS method calculation results, it can be found that the numerical calculation results are more accurate for the analysis ability under a large flow rate, and the mainstream velocity distribution is in good agreement. However, the RANS calculation results all amplify the analytical ability of the local low-speed vortex area. As a result, the calculation results of the low-speed range are larger than the test results.

(a)

(b)

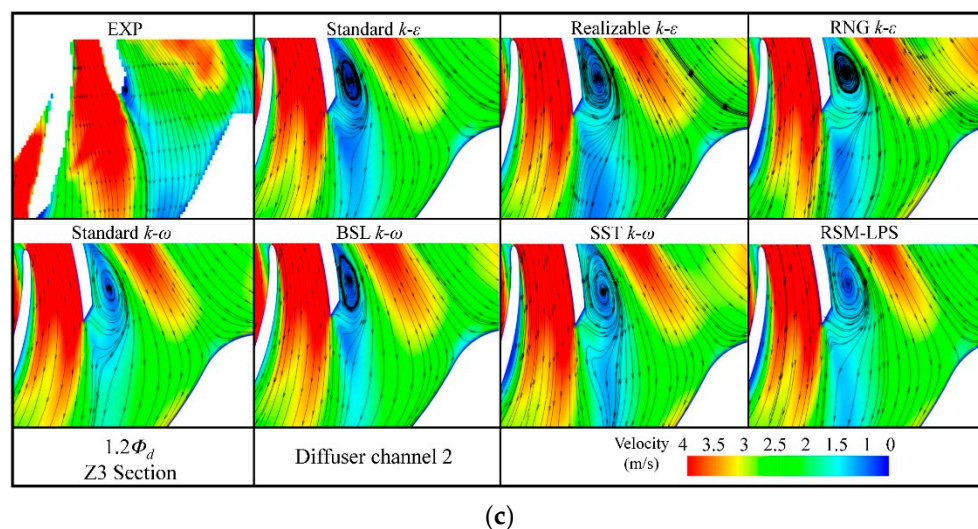**Figure 12.** *Cont.*

(c)
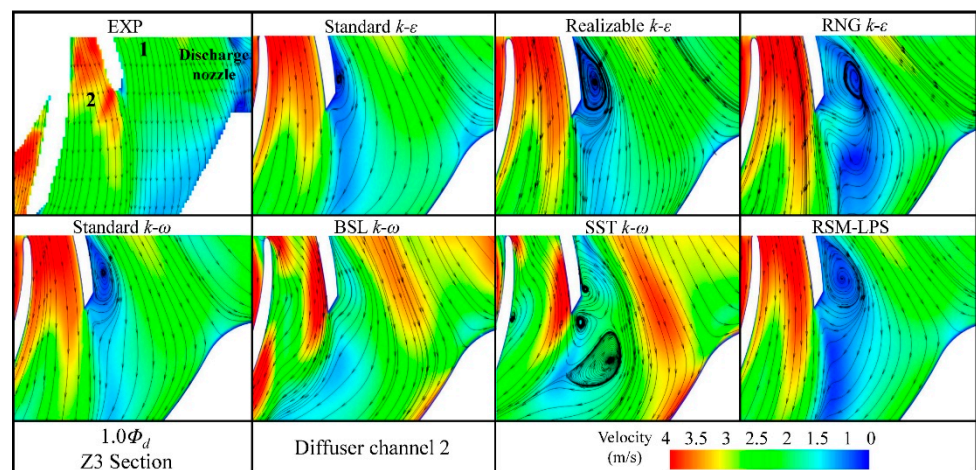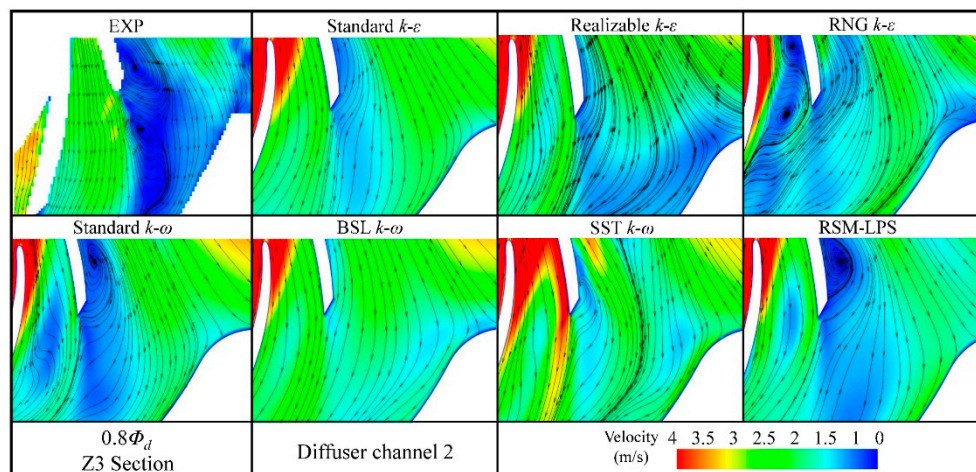
Figure 12. Internal velocity distribution of the experimental result and different RANS methods at Z3 section in diffuser flow channel 2. (**a**) 1.0 Φ_d; (**b**) 0.8 Φ_d; (**c**) 1.2 Φ_d.

To further quantitatively compare the velocity errors, Figure 13 shows the velocity distribution at the three main monitoring lines in the measurement area of diffuser flow channel 2 under the rated conditions. From Figure 13a,b, when X = 55 and X = 65, Y/L change from 0 to 1, the test result of the velocity value shows a gradually increasing trend. From the numerical simulation results, the Standard k-ε, Realizable k-ε and Standard k-ω models are relatively consistent with the experimental measurement results. However, the other turbulence models have larger errors. When X = 75 (Figure 13c), the velocity value measured by the experiment still shows a gradually increasing trend. In the area of $0.6 \le Y/L \le 0.95$, the RNG k-ε model is in good agreement with the experimental measured values. In the area of $Y/L \le 0.6$, the numerical simulation result is quite different from the experimental measurement.

Comprehensive analyses of Figures 12 and 13 show that the k-ε model (Standard k-ε, Realizable k-ε, RNG k-ε), Standard k-ω and RSM-LPS models have basically the same analytical capabilities for the complex flow at diffuser flow channel 2 and the discharge nozzle of the RCP based on the PIV measurement results under the nominal flow rate. However, the flow fields predicted by the BSL k-ω model and the SST k-ω model are quite different from the experimental measurement results. For the low flow rate, the flow field predicted by numerical calculation is quite different from the measured results, and the vortex-shedding structure in the local low-speed area of the diffuser trailing edge cannot be well analyzed. Under the large flow rate, the analytical capabilities for the flow field of the different turbulent models are basically the same, but the ability to analyze the local low-speed area of the diffuser trailing edge is magnified. Comprehensive analysis found that for the flow in the diffuser flow channel 2 and the discharge nozzle, the Realizable k-ε model can better analyze the flow field except for the low flow rate.

Through detailed qualitative and quantitative comparisons between the numerical calculation results of different turbulence models and the PIV results of the experimental measurement, the analysis shows that the PIV results and the RANS calculation results have the following errors:

1. To facilitate the comparison, a standard wall function is used in the RANS calculation. Therefore, the numerical calculation results show that the capture of flow field information near the wall is obviously insufficient. In addition, in this paper, only the external energy performance is verified in the verification of the mesh sensitivity. After the analysis and verification of this paper, it is believed that in the future, both external characteristics and internal flow characteristics should be verified simultaneously;

2. For PIV measurement, even though a water jacket is used to compensate for the refraction and scattering of light in the spherical casing caused by the large curvature, there will be a certain velocity measurement error in the near-wall area;

3. Considering the economics of the calculation, the gap between the mouth ring is ignored in the numerical calculation. Although the gap between the mouth ring is small to ensure consistency, there is still a small amount of leakage;

4. As the post-processing of PIV data adopts a moving average verification method for the original vector diagram, this method slightly smoothens the speed difference between the wake area vector and the surrounding vector [40,41]. In addition, the ability of the RANS method to identify the vortex region is magnified. These two factors have caused a large gap between the numerical calculation and the experimental measurement in the diffuser blade trailing edge region.
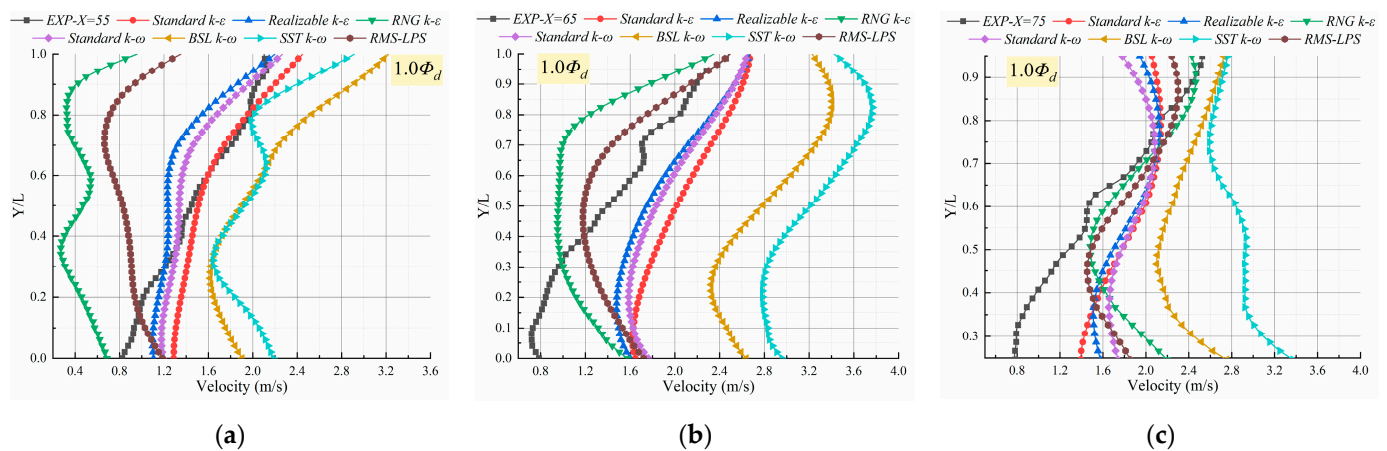

Figure 13. Velocity distribution of monitoring lines with diffuser channel 2 under 1.0 Φ_d. (**a**) X = 55; (**b**) X = 65; (**c**) X = 75.

5. Conclusions

Based on the energy performance test and Particle Image Velocimetry (PIV) flow field measurement results, a nuclear reactor coolant pump (RCP) model pump is analyzed respectively from the perspectives of energy performance and internal flow. Meanwhile, the numerical calculation accuracy of the different turbulence models is compared. Furthermore, the error analysis of the numerical calculation and test results is carried out. The real internal flow field and flow mechanism in the RCP are fully revealed, and a better RANS turbulence model for the RCP with a special structure is obtained. Some conclusions are made.

When the RCP is operating under the main operating conditions (0.8~1.2 Φ_d), the maximum error in energy performance of different RANS models is less than 10%, and the minimum error is less than 0.1%. Therefore, each turbulence model has the ability to predict the energy performance of RCP in the engineering applications.

From the measurement results of PIV, there is a large difference in velocity between the left and right sides of the discharge nozzle of the RCP. Due to the influence of vortex, backflow and large-scale flow-separation structure on the right side, the velocity is low and uneven. The fluid on the left side flows out of the discharge nozzle smoothly under the action of the main flow (through flow). In addition, the velocity distribution is relatively uniform and there is no obvious low-speed area.

Through the quantitative and qualitative comparison between the RANS method and experimental measurement of the internal flow field, it is found that under the nominal flow rate, the analytical capabilities of the *k-ε* model, Standard *k-ω* and RSM-LPS model are basically the same for the flow field. In addition, the results of the BSL *k-ω* model and the SST *k-ω* model are obviously inconsistent with the experimental results. Under the low flow rate, none of the models can precisely predict the internal flow field well. Under a

large flow rate, the analytical capabilities of the various calculation models for the flow field are basically the same, but the ability to analyze the local low-speed area of the diffuser blade trailing edge is magnified. It is generally believed that the Realizable *k-ε* model can better predict the internal flow field of the RCP compared with other turbulence models in this paper.

Finally, based on the current grid size and computing capabilities, we have analyzed the errors between the experimental measurement and numerical calculations. We believe that the accuracy of numerical calculation can still be improved in engineering applications, and we hope that our research results can provide a useful reference for further accurate prediction of the internal flow field of the RCP in the future. Furthermore, phase transition may occur in the coolant pump [42,43], and the phase equilibrium analysis can be involved in future studies to carry out more in-depth research of RCP.

Author Contributions: Methodology, D.N.; validation, H.L.; investigation, S.H.; resources, S.L.; data curation, Y.Z.; supervision, D.N. All authors have read and agreed to the published version of the manuscript.

Data Availability Statement: Not applicable.

Conflicts of Interest: The authors declare no conflict of interest in the paper.

Abbreviations

Acronyms	
RCP	Reactor Coolant Pump
NPP	Nuclear Power Plant
PIV	Particle Image Velocimetry
LDV	Laser Doppler Velocimetry
CFD	Computational Fluid Dynamics
DDES	Delayed Detached Eddy Simulation
PWR	Pressurized Water Reactor
RANS	Reynolds-Averaged Navier–Stokes
RSM	Reynolds Stress Model
MRF	Moving Reference Frame
Symbols	
Φ_d	Nominal flow coefficient
Ψ_d	Nominal head coefficient
n_d	Nominal rotating speed
n_s	Specific speed
D_1	Impeller inlet diameter
D_2	Impeller outlet diameter
b_2	Impeller outlet width
Ψ	head coefficient

References

1. Shindell, D.; Ru, M.; Zhang, Y.; Seltze, K.; Faluvegi, G.; Nazarenko, L.; Schmidt, G.A.; Parsons, L.; Challapalli, A.; Yang, L.; et al. Temporal and spatial distribution of health, labor, and crop benefits of climate change mitigation in the United States. *Proc. Natl. Acad. Sci. USA* **2021**, *118*, e2104061118. [CrossRef]
2. *Climate Change 2022: Impacts, Adaptation and Vulnerability Summary for Policymakers*; IPCC (Intergovernmental Panel on Climate Change): Geneva, Switzerland, 2022.
3. Kober, T.; Schiffer, H.-W.; Densing, M.; Panos, E. Global energy perspectives to 2060—WEC's World Energy Scenarios 2019. *Energy Strategy Rev.* **2020**, *31*, 100523. [CrossRef]

4. John, B.; Shannon, B.-S.; Wesley, C.; Brent, D.; Erich, E.; Jonathan, H.; Augustine, K.; Laura, M.; Caitlin, M.; Christopher, N.; et al. Modeling nuclear energy's future role in decarbonized energy systems. *iScience* **2023**, *26*, 105952. [CrossRef]

5. Roman, D. Nuclear and New Energy Technology. *Energies* **2022**, *15*, 6046. [CrossRef]

6. Sayed, M.S.; El-Mongy, S.A.; Tawfic, A.F.; Abdel-Rahman, M.A.E. Validation of the Optimized Parameters for Improvement of Gamma Spectrometers Performance and Efficacy. *Phys. Part. Nucl. Lett.* **2021**, *18*, 222–231. [CrossRef]

7. Ali Mohamed, A.E.M.; Tawfic, A.F.; Abdelgawad, M.A.; Mahdy, M.; Omar, A. Gamma and neutrons shielding using innovative fiber reinforced concrete. *Prog. Nucl. Energy* **2022**, *145*, 104133. [CrossRef]

8. Ali Mohamed, A.E.M.; Tawfic, A.F.; Abdelgawad, M.A.; Mahdy, M.; Omar, A. Potential uses of different sustainable concrete mixtures in gamma and neutrons shielding purposes. *Prog. Nucl. Energy* **2023**, *157*, 104598. [CrossRef]

9. Gao, H.; Gao, F.; Zhao, X.; Chen, J.; Cao, X. Analysis of reactor coolant pump transient performance in primary coolant system during start-up period. *Ann. Nucl. Energy* **2013**, *54*, 202–208. [CrossRef]

10. Ni, D.; Yang, M.; Zhang, N.; Gao, B.; Li, Z. Unsteady flow structures and pressure pulsations in a nuclear reactor coolant pump with spherical casing. *J. Fluids Eng. Trans. ASME* **2017**, *139*, 051103. [CrossRef]

11. Zhou, Q.; Li, H.; Pei, L.; Zhong, Z. Research on non-uniform pressure pulsation of the diffuser in a nuclear reactor coolant pump. *J. Nucl. Eng. Technol.* **2021**, *53*, 1020–1028. [CrossRef]

12. Zhang, N.; Zheng, F.; Liu, X.; Gao, B.; Li, G. Unsteady flow fluctuations in a centrifugal pump measured by laser Doppler anemometry and pressure pulsation. *Phys. Fluids* **2020**, *32*, 125108. [CrossRef]

13. Chen, B.; Li, X.; Zhu, Z. Investigations of energy distribution and loss characterization in a centrifugal impeller through PIV experiment. *Ocean. Eng.* **2022**, *247*, 110773. [CrossRef]

14. Feng, J.; Benra, F.-K.; Dohmen, H. Investigation of periodically unsteady flow in a radial pump by CFD simulations and LDV measurements. *J. Turbomach.* **2011**, *133*, 011004. [CrossRef]

15. Ni, D.; Zhang, N.; Gao, B.; Li, Z.; Yang, M. Dynamic measurements on unsteady pressure pulsations and flow distributions in a nuclear reactor coolant pump. *Energy* **2020**, *198*, 117305. [CrossRef]

16. Wu, Y.; Liu, S.; Yuan, H.; Shao, J. PIV measurement on internal instantaneous flows of a centrifugal pump. *Sci. China Technol.* **2011**, *54*, 270–276. [CrossRef]

17. Ofuchi, E.M.; Henrique, S.; Ernesto, M.; Rigoberto, E.M.M. Investigation of the flow field in a centrifugal rotor through particle image velocimetry. *Exp. Therm. Fluid Sci.* **2023**, *140*, 110768. [CrossRef]

18. Nicholas, P.; Larsen, P.S.; Jacobsen, C.B. Flow in a centrifugal pump impeller at design and off-design conditions-part I: Particle image velocimetry (PIV) and laser doppler velocimetry (LDV) measurements. *J. Fluids Eng. Trans. ASME* **2003**, *125*, 61–72. [CrossRef]

19. Sugiyama, D.; Ichinose, A.; Takeda, T.; Miyagawa, K.; Negishi, H.; Tsunoda, A. Investigation of Internal Flow in Centrifugal Pump Diffuser using Laser Doppler Velocimetry (LDV) and Computational Fluid Dynamics. *J. Phys. Conf. Ser.* **2021**, *1909*, 012075. [CrossRef]

20. Fu, S.; Zheng, Y.; Kan, K.; Chen, H.; Han, X.; Liang, X.; Liu, H.; Tian, X. Numerical simulation and experimental study of transient characteristics in an axial flow pump during start-up. *Renew. Energy* **2020**, *146*, 1879–1887. [CrossRef]

21. Zhang, N.; Liu, X.; Gao, B.; Wang, X.; Xia, B. Effects of modifying the blade trailing edge profile on unsteady pressure pulsations and flow structures in a centrifugal pump. *Int. J. Heat. Fluid Flow* **2019**, *75*, 227–238. [CrossRef]

22. Ge, C.Y.; Wang, J.J.; Gu, X.P.; Feng, L.F. CFD simulation and PIV measurement of the flow field generated by modified pitched blade turbine impellers. *Chem. Eng. Res. Des.* **2014**, *92*, 1027–1036. [CrossRef]

23. Li, H.; Chen, Y.; Yang, Y.; Wang, S.; Bai, L.; Zhou, L. CFD Simulation of Centrifugal Pump with Different Impeller Blade Trailing Edges. *J. Mar. Sci. Eng.* **2023**, *11*, 402. [CrossRef]

24. Giridharan, G.A.; Lederer, C.; Berthe, A.; Goubergrits, L.; Hutzenlaub, J.; Slaughter, M.S.; Dowling, R.D.; Spence, P.A.; Koenig, S.C. Flow dynamics of a novel counterpulsation device characterized by CFD and PIV modeling. *Med. Eng. Phys.* **2011**, *33*, 1193–1202. [CrossRef]

25. Ni, D.; Wang, F.; Gao, B.; Zhang, Y.; Huang, S. Experimental Investigation on the Effect of the Staggered Impeller on the Unsteady Pressure Pulsations Characteristic in a Pump. *Energies* **2022**, *15*, 8912. [CrossRef]

26. Ni, D.; Chen, J.; Wang, F.; Zheng, Y.; Zhang, Y.; Gao, B. Investigation into Dynamic Pressure Pulsation Characteristics in a Centrifugal Pump with Staggered Impeller. *Energies* **2023**, *16*, 3848. [CrossRef]

27. Zhang, N.; Jiang, J.; Gao, B.; Liu, X. DDES analysis of unsteady flow evolution and pressure pulsation at off-design condition of a centrifugal pump. *Renew. Energy* **2020**, *153*, 193–204. [CrossRef]

28. Yang, Z.; Wang, F.; Zhou, P. Evaluation of Subgrid-scale Models in Large-eddy Simulations of Turbulent Flow in a Centrifugal Pump Impeller. *Chin. J. Mech. Eng.* **2012**, *15*, 911–918. [CrossRef]

29. Zhang, Z.; Chen, H.; Yin, J.; Ma, Z.; Gu, Q.; Lu, J.; Liu, H. Unsteady flow characteristics in centrifugal pump based on proper orthogonal decomposition method. *Phys. Fluids* **2021**, *075122*, 075122. [CrossRef]

30. Salmani, F.; Rad, E.A.; Mahpeykar, M.R. Investigation effects of roughness in wet steam flow with Buckingham Pi-theorem. *J. Therm. Anal. Calorim.* **2022**, *147*, 3803–3813. [CrossRef]

31. Wilcox, D.C. *Turbulence Modeling for CFD*, 3rd ed.; DCW Industries: La Canada Flintridge, CA, USA, 2006.

32. Launder, B.E.; Spalding, D.B. *Lectures in Mathematical Models of Turbulence*; Academic Press: London, UK, 1972.

33. Yakhot, V.; Orszag, S.A. Renormalization group analysis of turbulence. I. Basic theory. *J. Sci. Comput.* **1986**, *1*, 3–51. [CrossRef]

34. Shih, T.-H.; Liou, W.W.; Shabbir, A.; Yang, Z.; Zhu, J. A new k-ε eddy viscosity model for high reynolds number turbulent flows. *Comput. Fluids* **1995**, *24*, 227–238. [CrossRef]

35. Wilcox, D.C. Multiscale model for turbulent flows. *AIAA J.* **1988**, *26*, 1311–1320. [CrossRef]

36. Menter, F.R. Two-equation eddy-viscosity turbulence models for engineering applications. *AIAA J.* **1994**, *32*, 1598–1605. [CrossRef]

37. Ni, D.; Yang, M.; Gao, B.; Zhang, N.; Li, Z. Flow unsteadiness and pressure pulsations in a puclear reactor coolant pump. *Strojniški Vestn.—J. Mech. Eng.* **2016**, *62*, 231–242. [CrossRef]

38. Ni, D.; Yang, M.; Gao, B.; Zhang, N.; Li, Z. Numerical study on the effect of the diffuser blade trailing edge profile on flow instability in a nuclear reactor coolant pump. *Nucl. Eng. Des.* **2017**, *322*, 92–103. [CrossRef]

39. Ni, D.; Yang, M.; Gao, B.; Zhang, N.; Li, Z. Experimental and numerical investigation on the pressure pulsation and instantaneous flow structure in a nuclear reactor coolant pump. *Nucl. Eng. Des.* **2018**, *337*, 261–270. [CrossRef]

40. Feng, J.; Benra, F.-K.; Dohmen, H.J. Unsteady Flow Visualization at Part-Load Conditions of a Radial Diffuser Pump: By PIV and CFD. *J. Vis.* **2009**, *12*, 65–72. [CrossRef]

41. Zhou, L.; Shi, W.; Cao, W.; Yang, H. CFD investigation and PIV validation of flow field in a compact return diffuser under strong part-load conditions. *Sci. China Technol. Sci.* **2015**, *58*, 405–414. [CrossRef]

42. Zhang, T.; Zhang, Y.; Katterbauer, K.; Al Shehri, A.; Sun, S.; Hoteit, I. Phase equilibrium in the hydrogen energy chain. *Fuel* **2022**, *15*, 328. [CrossRef]

43. He, Z.; Zhao, Z.; Zhang, X.; Feng, H. Thermodynamic properties of new heat pump working pairs: 1,3-Dimethylimidazolium dimethylphosphate and water, ethanol and methanol. *Fluid Phase Equilibria* **2010**, *298*, 83–91. [CrossRef]